Instantaneous velocity displacement and contour measurement by use of shadow moiré and temporal wavelet analysis

Tay, Cho Jui; Quan, Chenggen; Fu, Yu; Huang, Yuanhao

Instantaneous velocity displacement and contour measurement by use of shadow moiré and temporal wavelet analysis

Cho Jui Tay, Chenggen Quan, Yu Fu, and Yuanhao Huang

A temporal wavelet analysis method is proposed for velocity, displacement, and three-dimensional surface-profile measurement of a continuously deforming object by use of the shadow moiré technique. A grating is placed close to a deforming object, and its shadow is observed through the grating. The moiré fringe patterns, generated by the interference of the grating lines and their shadows, are captured by a high-speed CCD camera with a telecentric gauging lens. Instantaneous frequency of gray-value variation is evaluated point by point with the continuous wavelet transform. From the instantaneous frequency of each point on the object, the velocity, displacement, and high-quality surface profile at different instants can be retrieved. In this application, two specimens are tested to demonstrate the validity of the proposed method: One is a small coin with a rigid body motion, and the other is a simply supported beam subjected to a central point load. The results are compared with those obtained from temporal Fourier-transform and mechanical stylus methods. © 2004 Optical Society of America

OCIS codes: 100.7410, 120.4120, 100.5070, 120.6650.

1. Introduction

Moiré topography, which was proposed by Meadows *et al.*[1] and Takasaki[2] in the early 1970's, has been widely applied in industry for three-dimensional (3-D) profile measurement and surface analysis. Generally, it is classified into two types[3–5]: projection moiré and shadow moiré, according to the optical arrangement of the system. In projection moiré the fringe pattern is generated by one's projecting a grating onto the object and viewing it through a second grating. In shadow moiré the fringe pattern is generated by the interference of the grating lines and their shadows. It is a relatively simple technique that uses a single grating placed close to the object. One shortcoming of the shadow moiré is the difficulty of determining whether the surface is convex or concave from one fringe pattern.[6] This is also a difficulty encountered with other optical techniques. Compared with other interferometric techniques, the moiré technique is also less sensitive. To achieve high-resolution measurements, researchers applied different types of phase-shifting technique in moiré topography[7–12] in the 1990's. However, the phase-shifting methods were limited to surface contouring of static objects only.

The moiré technique has also been applied to dynamic problems by use of the time-averaged method.[13–16] In these studies, vibration amplitude is determined from time-averaged fringe patterns. However, they did not apply the method to study the instantaneous displacement and contour of an object as a function of time. In many cases, high-resolution 3-D dynamic surface profiling of objects with continually changing profiles gives useful information on the dynamic response and deformation of the objects.

In the late 1990's, temporal phase-analysis and temporal phase-unwrapping techniques[17–19] were introduced to study continuously deformed objects.[20–22] Other applications involve contouring surface with discontinuities by wavelength-scanning interferometry.[23,24] Jin *et al.*[25] applied the same concept by using the shadow moiré technique to retrieve point-by-point height information with a frequency sweeping method. The moiré patterns are varied by a rotating grating, and a series of fringe patterns are obtained. By one's applying the Fourier-transform method along a time axis, the frequency of intensity

variation at each point is obtained; subsequently, the height of each point is determined without the need for spatial phase unwrapping. This method is more suitable for measuring objects with discontinuities such as step changes or spatially isolated surfaces.

Among temporal phase-analysis algorithms,[26] the Fourier-transform method[27] is the most popular method. The intensity fluctuation due to deformation of each pixel is first transformed, and one side of the spectrum is filtered with a bandpass filter. The filtered spectrum is inverse transformed to obtain the wrapped phase. The phase values are then unwrapped along the time axis at each pixel. The accuracy of the Fourier-transform analysis increases with higher temporal frequency for a narrow spectrum. However, in most cases the deformation of each point on an object is different, and the deformation of each point may also be nonlinear along the time axis. An automatic filtering process becomes difficult as the width of the bandpass filter has to be broadened and introduces further errors in phase extraction. This shortcoming of Fourier analysis can be overcome by the use of the wavelet transform.

The wavelet transform[28] is a new and robust mathematic tool for signal analysis. The continuous wavelet transform (CWT) was also used for phase extraction on different types of fringe pattern with spatial carriers.[29–31] These applications use one-dimensional CWT along a spatial axis. The instantaneous frequency of gray-value variation can be obtained by one's extracting the ridge of the wavelet coefficients, which is followed by an integration process to retrieve the phase. The CWT also gains applications in analyzing moiré fringe patterns.[32–34] However, all these techniques extract the phase in the spatial domain.

The wavelet transform has also been applied to temporal phase analysis of speckle interferometry. The concept was first introduced by Colonna de Lega in 1996, and some preliminary results were presented.[35,36] In this study, temporal wavelet analysis is applied to retrieve the instantaneous velocity, displacement, and contour of objects from a series of shadow moiré fringe patterns captured by a high-speed CCD camera. Two specimens are selected to demonstrate the validity of the proposed method. One is a simply supported beam with central-point loading. The velocity and displacement on each point are different. The velocity can be retrieved directly from an instantaneous frequency on the ridge; integration is then carried out to obtain the displacement. Neither temporal nor spatial phase unwrapping is needed for displacement measurement. However, in most cases, spatial phase unwrapping is still necessary when the instantaneous contour is reconstructed. To verify the accuracy of instantaneous surface profiling, we subject a small coin to a rigid body motion. The retrieved surface profile is compared with results from the mechanical stylus method.
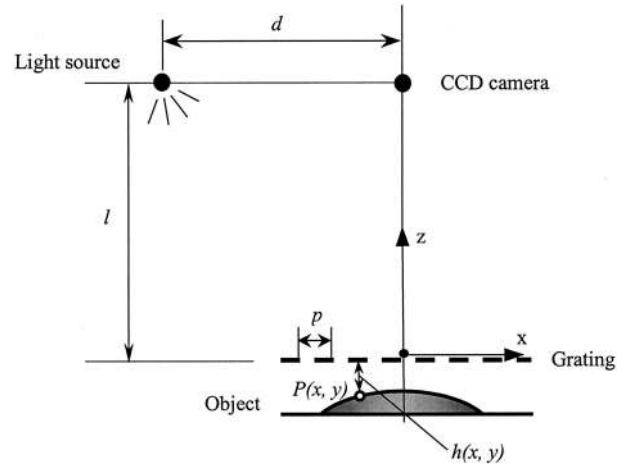

Fig. 1. Schematic layout of the shadow moiré system.

2. Theoretical Analysis

Figure 1 shows the optical arrangement. A grating is placed in the x–y plane and is close to the object surface. A camera and a light source are placed at distance l from the grating with a pitch p. The intensity distribution captured by a CCD camera is governed by the following equation[25]:

$$I(x, y) = a(x, y) + b(x, y)\cos\left\{\frac{2\pi h(x, y)d}{p[l + h(x, y)]}\right\}, \quad (1)$$

where $a(x, y)$ and $b(x, y)$ are the intensity bias and modulation factor, respectively. d is the distance between the light source and the camera, $h(x, y)$ is the distance from the grating plane to a point $P(x, y)$. In normal cases, $l \gg h(x, y)$, Eq. (1) can be simplified as

$$I(x, y) = a(x, y) + b(x, y)\cos[kh(x, y)], \quad (2)$$

where $k = 2\pi d/pl$ is a constant related to the optical setup.

When the object deforms in the z direction, Eq. (2) can be rewritten as

$$\begin{aligned} I(x, y; t) &= a(x, y; t) + b(x, y; t)\cos[\phi_{xy}(t)] \\ &= a(x, y; t) + b(x, y; t)\cos\{k[h(x, y; t) \\ &\quad + h_0(x, y)]\}, \end{aligned} \quad (3)$$

where $h_0(x, y)$ is the initial distance between the grating and a point on the object. $h(x, y; t)$ is a time-dependent distance of a point as the object deforms. Both $a(x, y; t)$ and $b(x, y; t)$ are slowly varying functions of time. A series of fringe patterns are recorded during deformation, and, at each pixel, the history of intensity variation is analyzed by the CWT.

The CWT of a signal $s(t)$ is defined as its inner product with a family of wavelet function $\Psi_{a,b}(t)$:

$$W_S(a, b) = \int_{-\infty}^{+\infty} s(t)\Psi_{a,b}{}^*(t)\mathrm{d}t, \quad (4)$$

where * denotes the complex conjugate. Given a mother wavelet $\Psi(t)$, a family $\Psi_{a,b}(t)$ can be constructed by elementary operations consisting of time shifts and scaling (i.e., dilation or contraction). The family of wavelets is defined by

$$\Psi_{a,b}(t) = \frac{1}{\sqrt{a}} \psi\left(\frac{t-b}{a}\right), \qquad b \in R, a > 0, \quad (5)$$

where a is the scaling factor and b is the time shift. The signal $s(t)$ can be recovered from the wavelet coefficients $W_S(a, b)$ by an inverse wavelet transform given by

$$s(t) = \frac{1}{C_\Psi} \int_{-\infty}^{+\infty} \int_0^{+\infty} W_S(a, b) \psi\left(\frac{t-b}{a}\right) \frac{\mathrm{d}a}{a^2} \, \mathrm{d}b, \quad (6)$$

provided that the constant C_Ψ is given by

$$C_\Psi = \int_{-\infty}^{+\infty} \frac{|\hat{\Psi}(\omega)|^2}{\omega} \, \mathrm{d}\omega < +\infty, \qquad (7)$$

where $\hat{\Psi}(\omega)$ denotes the Fourier transform of $\Psi(t)$. The mother wavelet function $\Psi(t)$ is a zero-mean wiggle (real or complex), localized both in time and in frequency, and it satisfies the admissibility condition given by expression (7).

For analysis of phase-related properties of real functions (e.g., determination of instantaneous frequency), the complex CWT is more suitable than the real wavelet transform or the discrete wavelet transform. The most commonly used mother wavelet for such applications is the complex Morlet wavelet because it gives the smallest Heisenberg box[37]:

$$\Psi(t) = g(t)\exp(i\omega_0 t), \qquad (8)$$

where $g(t) = \exp(-t^2/2)$. Here $\omega_0 = 2\pi$ is chosen to satisfy the admissibility condition so that the wavelet function is able to remove the negative frequencies as well as avoid the dc contribution of the signals. In this study the CWT expands a one-dimensional temporal intensity variation of certain pixels into a two-dimensional plane of scaling a (which is related to the temporal frequency) and position b (which is related to the time axis). One shortcoming of the CWT is the large error generated at the boundary of the signal. To overcome this problem, we extend the signal at its left- and right-hand edges. Instead of the commonly adopted symmetrical or zero-padding extension techniques, a linear predictive extrapolation method[30] is used in this study. The advantage of this extrapolation method is that the phase and frequency of intensity variations are maintained. After the CWT has been carried out on the extended data, the wavelet coefficients are truncated appropriately.

Substituting Eqs. (3) and (8) into Eq. (4), one can express the wavelet transform of the temporal intensity variation on pixel $P(x, y)$ as[37]

$$W_{xy}(a, b) = \frac{\sqrt{a}}{2} A_{xy}(b)(\hat{g}\{a[\zeta - \phi_{xy}'(b)]\}$$
$$+ \epsilon(b, \zeta))\{\exp[i\phi_{xy}(b)]\}, \qquad (9)$$

where $\zeta = \omega_0/a$ and ϵ is a corrective term that is negligible if the following conditions are satisfied:

$$\frac{\omega_0^2}{|\phi_{xy}'(b)|^2} \frac{|A_{xy}''(b)|}{|A_{xy}(b)|} \ll 1, \qquad (10)$$

$$\omega_0^2 \frac{|\phi_{xy}''(b)|}{|\phi_{xy}'(b)|^2} \ll 1. \qquad (11)$$

The trajectory of maximum $|W_{xy}(a, b)|^2$ on the a–b plane is called a ridge. Because $|\hat{g}(\omega)|$ is maximum at $\omega = 0$, and if $\epsilon(b, \zeta)$ is negligible, $|W_{xy}(a, b)|^2$ reaches maximum when

$$\phi_{xy}'(b) = \zeta_{rb} = \omega_0/a_{rb}, \qquad (12)$$

where $\phi_{xy}'(b)$ is defined as the instantaneous frequency of the signal and a_{rb} denotes the value of a at instant b on the ridge. The instantaneous velocity of point $P(x, y)$ at instant b can be retrieved directly from $\phi_{xy}'(b)$.

The wavelet transform on the ridge can then be expressed as

$$W_{xy}(a_{rb}, b) \approx \frac{\sqrt{a_{rb}}}{2} A_{xy}(b)\hat{g}(0)\exp[i\phi_{xy}(b)]. \quad (13)$$

The complex phase value Φ_W of wavelet transform $W_{xy}(a, b)$ on the ridge equals $\phi_{xy}(b)$, which represents the instantaneous distance between the grating and point $P(x, y)$ on the object. To retrieve the instantaneous contour of the object, we calculate the arctangent of the ratio of the imaginary and real parts of the wavelet transform on the ridge:

$$\phi_{xy}(b) = \tan^{-1}\left\{\frac{\mathrm{Im}[W_{xy}(a_{rb}, b)]}{\mathrm{Re}[W_{xy}(a_{rb}, b)]}\right\}, \qquad (14)$$

where Re and Im denote the real and imaginary parts of the wavelet transform. However, $\phi_{xy}(b)$ obtained from Eq. (14) is within $[0, 2\pi)$, and phase unwrapping on the spatial domain cannot be avoided. For the deformation measurement, the phase value $\phi_{xy}(b)$ is calculated by integration of the instantaneous frequency in Eq. (12), and the phase-unwrapping procedure is avoided in both the temporal and the spatial domains. The combination of phase values of each pixel at certain instant T generates a phase map of ϕ_T, and deformation between two instants T_1 and T_2 can be obtained by $(\phi_{T_2} - \phi_{T_1})$.

3. Experimental Illustration

Figure 2 shows the experimental setup. A simply supported Perspex beam is subjected to continuous deformation in the z direction by a motorized stage. A vertical sinusoidal grating with a frequency of 6
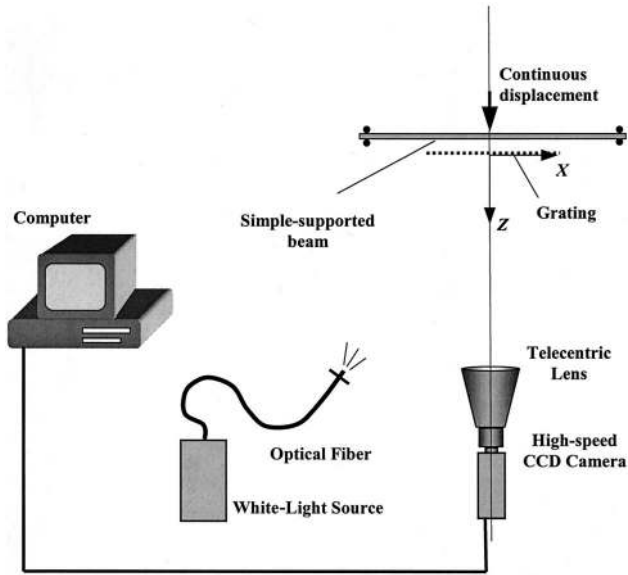
Fig. 2. Experimental setup.

lines/mm is positioned close to the beam. A 150-W dc white-light source with optical fiber illuminates the object at a certain angle. The moiré fringe patterns are captured at a right angle by a high-speed CCD camera. The magnification error on the object due to out-of-plane deformation can be eliminated by use of a telecentric gauging lens. As the imaging area is smaller than the telecentric lens, each point on the object is imaged at a right angle. In this case, the camera and the light source do not have to be placed at the same distance from the object as in Fig. 1. This will reduce error caused by misalignment.
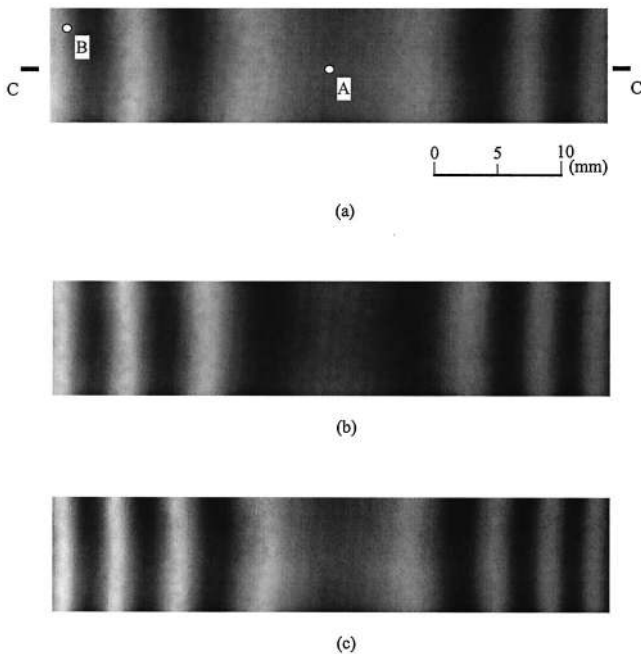

Fig. 3. Typical moiré fringe patterns of a simply supported beam at different instants: (a) 0.4 s, (b) 0.64 s, and (c) 0.88 s.
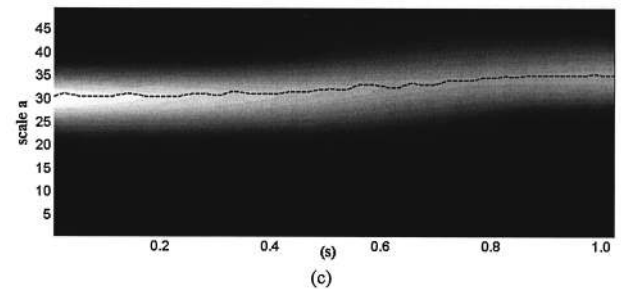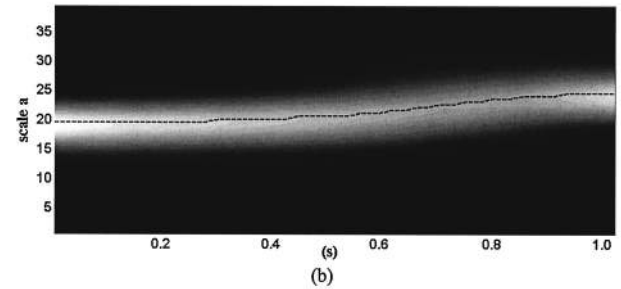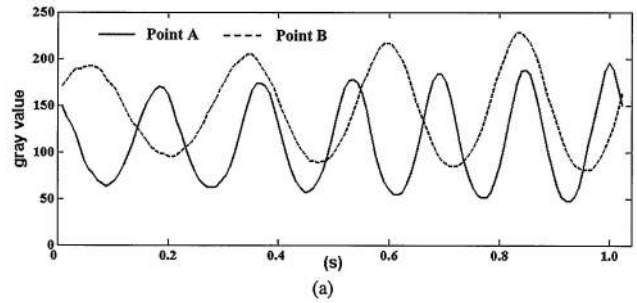

Fig. 4. (a) Gray values of points A and B. (b) Modulus of the Morlet wavelet transform at point A. (c) Modulus of the Morlet wavelet transform at point B.

As the direction of deformation is known, carrier fringes are not introduced in this experiment, and the grating is placed parallel to the beam.

In a subsequent experiment, a coin (specimen 2) is subjected to a rigid body motion in the z direction. To determine the absolute surface profile, we introduce carrier fringes by rotating the grating by a small angle in the x–z plane. As the angle of rotation is small, the variation of grating pitch due to the rotation is neglected.

4. Results and Discussion

Figure 3 shows three typical fringe patterns captured on a part of a simply supported beam at intervals of 0.008 s with an imaging rate of 125 frames/s (fps). Distances d and l (see Fig. 1) are 360 and 465 mm, respectively, and, as the grating is placed close to the object, the assumption of $l \gg h(x, y)$ is satisfied. Five hundred fringe patterns are captured during a 4-s period, and 128 consecutive images are selected for processing. At each pixel, 128 sampling points along the time axis are obtained. Figure 4(a) shows the gray-value variation of points A and B [see Fig. 3(a)]. Owing to the diffraction effect, the fringe con-
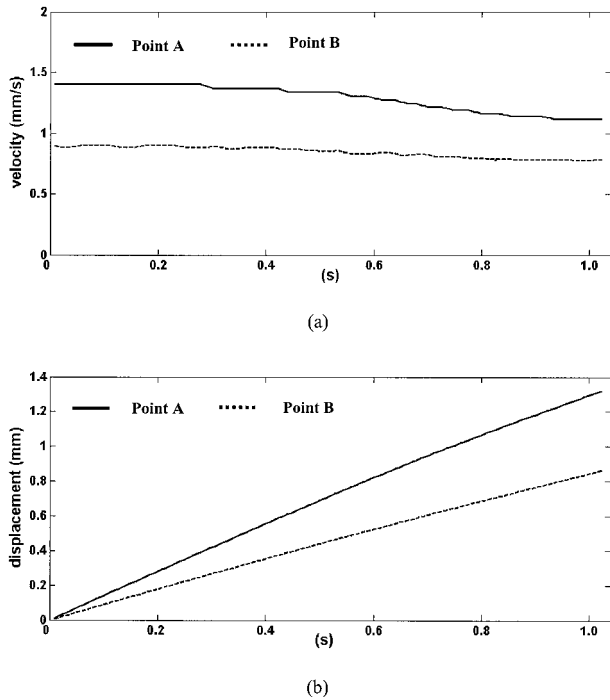
Fig. 5. (a) Instantaneous velocity and (b) displacement at points A and B.
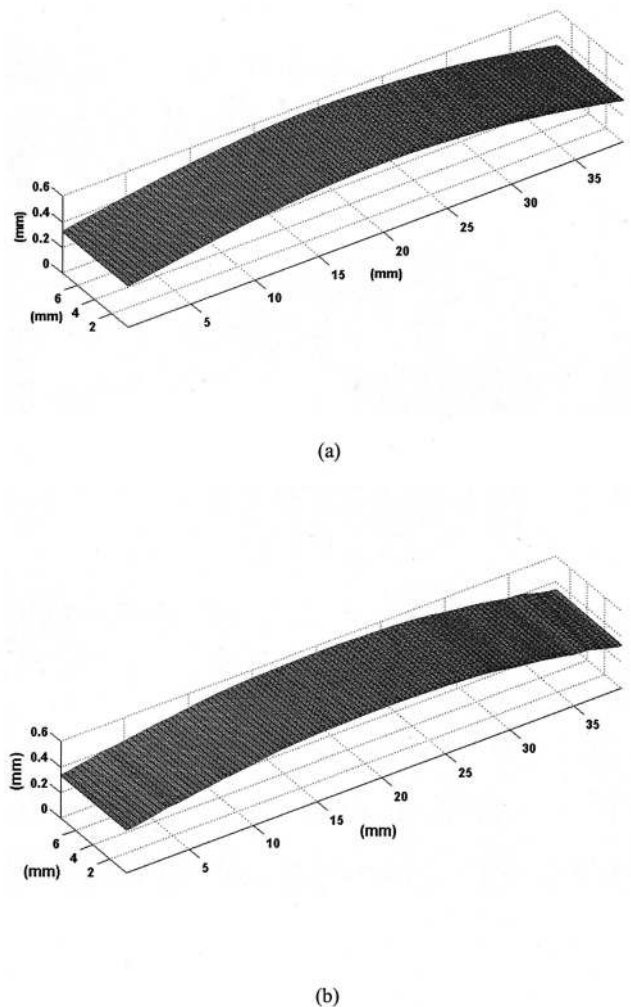

(a)

(b)

Fig. 6. Displacement of the beam between two instants $T_1 = 0.4$ s and $T_2 = 0.8$ s by use of (a) temporal wavelet analysis and (b) temporal Fourier analysis.

trast is low when the distance between the object and the grating is large. A slight increase in contrast is observed at both points A and B, which implies that distance $h(x, y; t)$ is decreasing. The error on phase extraction due to amplitude variation can be omitted as it is slow varying and expression (10) is satisfied. A slight difference in amplitude between points A and B is also observed due to nonuniform illumination and surface reflectivity. This will not affect the results as each pixel in the image is processed independently of one another. Only temporal frequencies are considered as they contain information on velocity and displacement. Compared with point B, higher temporal frequency is observed at point A. This implies that point A deforms faster than point B. The moduli of the Morlet wavelet transform of the intensity variation of points A and B are shown in Figs. 4(b) and 4(c), respectively. The dashed curve shows the ridge of the wavelet transformation in which the maximum moduli are found. Only a slight variation of a_{rb} is observed on the ridge, which implies that the velocities do not vary significantly along the time axis. The transient velocities of points A and B, obtained directly from the instantaneous frequency, are given in Fig. 5(a). Integration of $2\pi/a_{rb}$ is carried out on each pixel to obtain a continuous temporal displacement curve at each pixel [see Fig. 5(b)]. Displacement between any two instants T_1 and T_2 can be obtained from $(\phi_{T_2} - \phi_{T_1})$. Figure 6(a) shows a spatial displacement distribution within two instants $T_1 = 0.4$ s and $T_2 = 0.8$ s.

For comparison, temporal Fourier analysis is also applied to the same fringe patterns. As the displacements of each pixel are different, different frequency

spectra are expected. To cover all frequencies, we selected a relatively wider bandpass filter. The filtered spectrum is inverse transformed to obtain a wrapped phase. One-dimensional phase unwrapping is then applied to each pixel along the time axis. Figure 6(b) shows a 3-D displacement plot obtained by a temporal Fourier transform. Figure 7 shows a comparison of displacement on cross section C–C [see
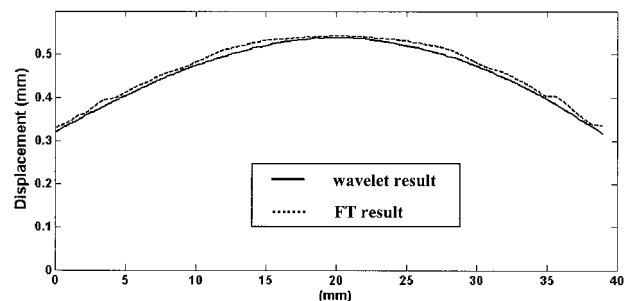

Fig. 7. Comparison of displacement at cross section C–C between wavelet and Fourier analyses. FT, Fourier transform.
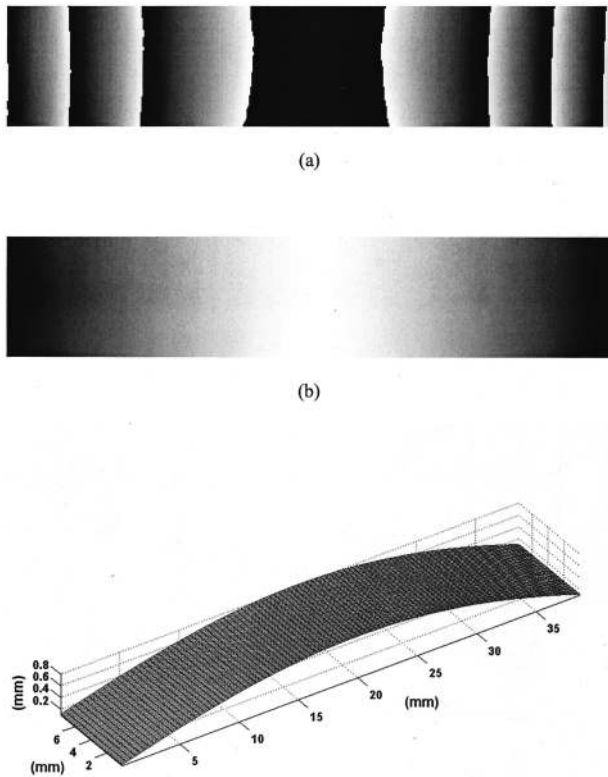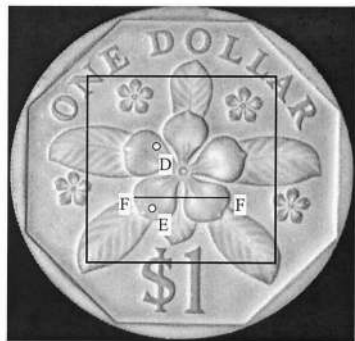
Fig. 8. (a) Wrapped phase map, (b) phase map after unwrapping, and (c) 3-D plot of instantaneous surface profile at $t_2 = 0.8$ s.
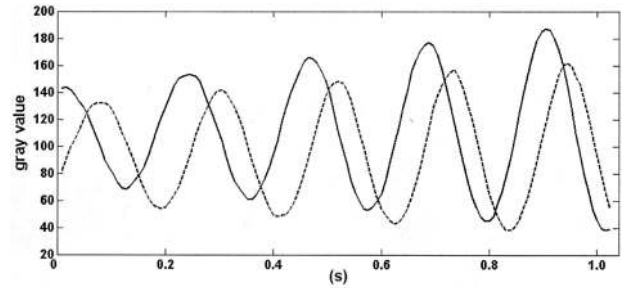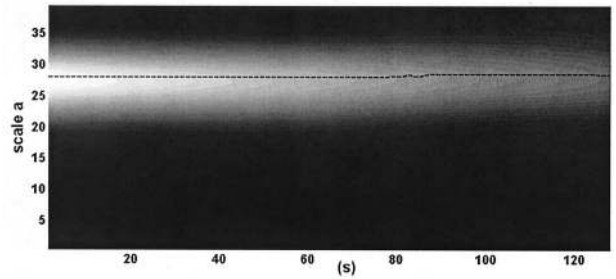

Fig. 9. (a) Area of interest on a coin (specimen 2) and typical moiré fringe patterns at (b) 0.4 s and (c) 0.8 s.

Fig. 10. (a) Gray values of points D and E. (b) Plot of moduli of Morlet wavelet transform at points D and E.

Fig. 3(a)]. It can be observed that results from these two methods agree well. However, the wavelet method provides a much smoother displacement map. The fluctuation in the Fourier transform is approximately 0.02 mm. However, the fluctuation is less than 0.01 mm in the wavelet method. From the comparison, it can be seen that more accurate displacements are obtained with the wavelet method. As the wavelet method calculates the optimized frequency at each instant, it performs an adaptive band-pass filtering of the measured signal and thus limits the influence of various noise sources and increases the resolution of the measurement significantly. In contrast, the Fourier-transform method uses a broader filter that is less efficient in eliminating the influence of noise.

To retrieve an instantaneous contour of the specimen, we use Eq. (14) to obtain a wrapped phase map [see Fig. 8(a)]. Figures 8(b) and 8(c) show, respectively, an unwrapped phase map in the spatial domain and a 3-D contour at instant $T = 0.8$ s. To verify the accuracy of the contour measurement, we subject a coin of 22.4-mm diameter with a diffused surface to a rigid body motion in the z axis [see Fig. 9(a)]. The distances d and l (see Fig. 1) are 300 and 450 mm, respectively, and the frequency of the grating is 6 lines/mm. The camera recording rate is 125 fps. Figures 9(b) and 9(c) show typical fringe patterns recorded at different instants. A carrier fringe is introduced by our slightly rotating the grating. We selected 128 consecutive images for processing from a total of 500 frames. Figure 10(a) shows the gray-value variation of points D and E. Although the initial phases of these two points are different,
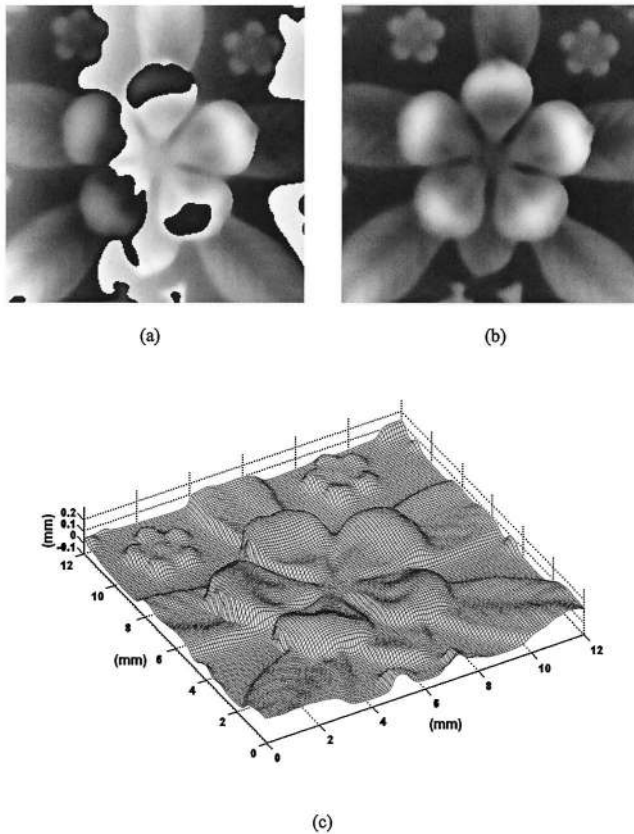
Fig. 11. (a) Wrapped phase map, (b) phase map after unwrapping, and (c) reconstructed 3-D plot of instantaneous surface profile of specimen 2 at $t_2 = 0.8$ s.
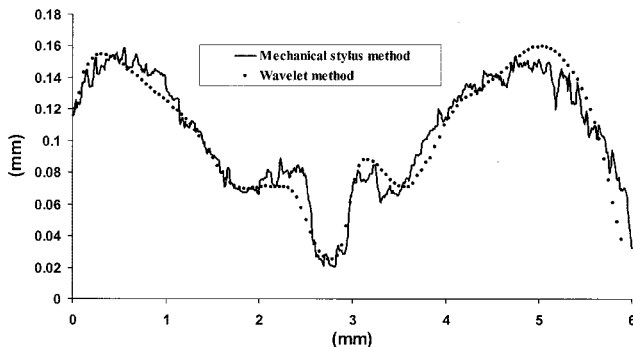

Fig. 12. Comparison of the surface profile of specimen 2 at cross section F–F between the wavelet and the mechanical stylus methods.

the frequencies of gray-value variation along the time axis are the same, which implies that these two points have similar velocities and displacements. The moduli of the Morlet wavelet transform of these two points are also the same, and one of them is shown in Fig. 10(b). Figures 11(a) and 11(b) show, respectively, a wrapped and unwrapped phase map at instant $T = 0.8$ s. In Fig. 11(b) the unwrapped phase has been subtracted from a base-plane value to remove the carrier effect. Figure 11(c) shows a 3-D reconstruction of the area of interest on the coin. Figure 12 shows a comparison of the profile on cross

section F–F [see Fig. 9(a)] by use of the proposed wavelet and mechanical stylus methods. The results generally agree well, and the maximum discrepancy is approximately 15 μm. This is of the same order of error as that of the phase-shifting method.[8–12] It should be noted, however, that in the phase-shifting method at least three images are required.

5. Concluding Remarks

In this paper a novel method based on temporal wavelet analysis is presented to retrieve transient velocity, displacement, and surface contour on a continuously deforming object. Unlike conventional temporal Fourier analysis, this method, which employs shadow moiré, extracts the instantaneous frequency point by point along the time axis with continuous Morlet wavelet transforms. Velocity can be retrieved directly from an instantaneous frequency, and a high-quality deformation map can also be obtained without any phase-unwrapping process. However, spatial phase unwrapping is still needed for the reconstruction of an instantaneous surface contour. A comparison between wavelet and Fourier analyses shows that the wavelet method can limit the influence of various noise sources and improve the results significantly. High-quality surface profiles can also be retrieved from a continuous deformed object, for which the normal phase-shifting method is not applicable. The results of contour measurement compared well with the mechanical stylus method, and the accuracy of the proposed method is of the order of 10 μm. Similar to the Fourier transform, the temporal wavelet method could also be applied to wavelength-scanning interferometry and other similar contouring techniques. It should gain more acceptance in speckle interferometry, as the influence of noise is much more serious on speckle patterns.

References

1. D. M. Meadows, W. O. Johnson, and J. B. Allen, "Generation of surface contours by moiré patterns," Appl. Opt. **9,** 942–947 (1970).
2. H. Takasaki, "Moiré topography," Appl. Opt. **9,** 1467–1472 (1970).
3. T. Tsuruta and Y. Itoh, "Interferometric generation of counter lines on opaque objects," Opt. Commun. **1,** 34–36 (1969).
4. J. Wasowski, "Moiré topographic maps," Opt. Commun. **2,** 321–323 (1970).
5. J. B. Allen and D. M. Meadows, "Removal of unwanted patterns from moiré contour maps by grid translation techniques," Appl. Opt. **10,** 210–212 (1971).
6. Y. Arai, S. Yokozeki, and T. Yamada, "Fringe-scanning method using a general function for shadow moiré," Appl. Opt. **34,** 4877–4882 (1995).
7. G. Mauvoisin, F. Bremand, and A. Lagarde, "Three-dimensional shape reconstruction by phase-shifting shadow moiré," Appl. Opt. **33,** 2163–2169 (1994).
8. X. Xie, M. J. Lalor, D. R. Burton, and M. M. Shaw, "Four-map absolute distance contouring," Opt. Eng. **36,** 2517–1520 (1997).
9. T. Yoshizawa and T. Tomisawa, "Shadow moiré topography by means of the phase-shift method," Opt. Eng. **32,** 1668–1674 (1993).

10. L. Jin, Y. Kodera, T. Yoshizawa, and Y. Otani, "Shadow moiré profilometry using the phase-shifting method," Opt. Eng. **39,** 2119–2123 (2000).

11. J. Degrieck, W. Van Paepegem, and P. Boone, "Application of digital phase-shift shadow moiré to micro deformation measurements of curved surface," Opt. Lasers Eng. **36,** 29–40 (2001).

12. R. Henan, A. Tagliaferri, and R. Torroba, "A contouring approach using single grating digital shadow moiré with a phase stepping technique," Optik **110,** 199–201 (1999).

13. J. D. Hovanesian and Y. Y. Hung, "Moiré contour-sum contour-difference, and vibration analysis of arbitrary objects," Appl. Opt. **10,** 2734–2738 (1971).

14. Y. Y. Hung, C. Y. Liang, J. D. Hovanesian, and A. J. Durelli, "Time-averaged shadow-moiré method for studying vibrations," Appl. Opt. **16,** 1717–1719 (1977).

15. B. Dessus and M. Leblanc, "The 'fringe method' and its application to the measurement of deformations, vibrations, contour lines and differences of objects," Opto-electronics **5,** 369–391 (1973).

16. J. Fujimoto, "Determination of the vibration phase by a time-averaged shadow moiré method," Appl. Opt. **21,** 4373–4376 (1982).

17. H. J. Tiziani, "Spectral and temporal phase evaluation for interferometry and speckle applications," in *Trends in Optical Nondestructive Testing and Inspection*, P. K. Rastogi and D. Inaudi, eds. (Elsevier Science, Oxford, UK, 2000), pp. 323–343.

18. J. M. Huntley and H. Saldner, "Temporal phase-unwrapping algorithm for automated interferogram analysis," Appl. Opt. **32,** 3047–3052 (1993).

19. J. M. Huntley, "Challenges in phase unwrapping," in *Trends in Optical Nondestructive Testing and Inspection*, P. K. Rastogi and D. Inaudi, eds. (Elsevier Science, Oxford, UK, 2000), pp. 37–44.

20. C. Joenathan, B. Franze, P. Haible, and H. J. Tiziani, "Speckle interferometry with temporal phase evaluation for measuring large-object deformation," Appl. Opt. **37,** 2608–2614 (1998).

21. C. Jonathan, B. Franze, P. Haible, and H. J. Tiziani, "Large in-plane displacement measurement in dual-beam speckle interferometry using temporal phase measurement," J. Mod. Opt. **45,** 1975–1984 (1998).

22. C. Jonathan, B. Franze, P. Haible, and H. J. Tiziani, "Novel temporal Fourier transform speckle pattern shearing interferometer," Opt. Eng. **37,** 1790–1795 (1998).

23. H. Tiziani, B. Franze, and P. Haible, "Wavelength-shift speckle interferometry for absolute profilometry using a mode-hop free external cavity diode laser," J. Mod. Opt. **44,** 1485–1496 (1997).

24. M. Takeda and H. Yamamoto, "Fourier-transform speckle profilometry: three-dimensional shape measurements of diffuse objects with large height steps and/or spatially isolated surfaces," Appl. Opt. **33,** 7829–7837 (1994).

25. L. H. Jin, Y. Otani, and T. Yoshizawa, "Shadow moiré profilometry by frequency sweeping," Opt. Eng. **40,** 1383–1386 (2001).

26. C. Quan, Y. Fu, and C. J. Tay, "Determination of surface contour by temporal analysis of shadow moiré fringes," Opt. Commun. **230,** 23–33 (2004).

27. M. Takeda, H. Ina, and S. Kobayashi, "Fourier-transform method of fringe-pattern analysis for computer-based topography and interferometry," J. Opt. Soc. Am. **72,** 156–160 (1982).

28. I. Daubechies, *Ten Lectures on Wavelets* (Society for Industrial and Applied Mathematics, Philadelphia, Pa., 1992).

29. L. R. Watkins, S. M. Tan, and T. H. Barnes, "Determination of interferometer phase distributions by use of wavelets," Opt. Lett. **24,** 905–907 (1999).

30. A. Federico and G. H. Kaufmann, "Evaluation of the continuous wavelet transform method for the phase measurement of electronic speckle pattern interferometry fringes," Opt. Eng. **41,** 3209–3216 (2002).

31. J. Fang, C. Y. Xiong, and Z. L. Yang, "Digital transform processing of carrier fringe patterns from speckle-shearing interferometry," J. Mod. Opt. **48,** 507–520 (2001).

32. Y. Morimoto, M. Fujigaki, and S. Yoneyama, "Shape, stress, and strain measurement using phase analysis of grating or fringe patterns," in *Third International Conference on Experimental Mechanics*, X. Wu, Y. Qin, J. Fang, and J. Ke, eds., Proc. SPIE **4537,** 47–52 (2002).

33. K. Qian, H. S. Seah, and A. Asundi, "Instantaneous frequency and its application to strain extraction in moiré interferometry," Appl. Opt. **42,** 6504–6513 (2003).

34. K. Kadooka, K. Kunoo, N. Uda, K. Ono, and T. Nagayasu, "Strain analysis for moiré interferometry using the two-dimensional continuous wavelet transform," Exp. Mech. **43,** 45–51 (2003).

35. X. Colonna de Lega, "Continuous deformation measurement using dynamic phase-shifting and wavelet transform," in *Applied Optics and Optoelectronics 1996*, K. T. V. Grattan, ed. (Institute of Physics, Bristol, UK, 1996), pp. 261–267.

36. M. Cherbuliez, P. Jacquot, and X. Colonna de Lega, "Wavelet processing of interferometric signals and fringe patterns," in *Wavelet Applications in Signal and Image Processing*, M. A. Unser, A. Aldroubi, A. F. Laine, eds., Proc. SPIE **3813,** 692–702 (1999).

37. S. Mallat, *A Wavelet Tour of Signal Processing* (Academic, San Diego, Calif., 1998).